Supplementary Information (SI) for Journal of Materials Chemistry A.

# Supplementary Information (SI)

# Mechanically and photoelectrochemically stable $WO_3$ | $BiVO_4$ | NiFeOOH photoanodes synthesised by a scalable chemical vapour deposition method

George Creasey,*[a,b] Tristan McCallum, [b] Guangrui Ai, [b] Brian Tam, [b] John Rodriguez Acosta, [a] Alvia Mohammad Yousuf, [b] Sarah Fearn, [c] Flurin Eisner, [d] Andreas Kafizas [b] and Anna Hankin *[a]

---

*[a] Department of Chemical Engineering, Imperial College London, South Kensington, London, SW7 2AZ.*
*[b] Department of Chemistry, The Molecular Science Research Hub, Imperial College London, White City, London, W12 0BZ..*
*[c] Department of Materials, Imperial College London, South Kensington, London, SW7 2AZ.*
*[d] School of School of Engineering and Materials Science, Queen Mary University of London, Bethnal Green, London, E1 4NS*
** Co-corresponding authors: g.creasey22@imperial.ac.uk and anna.hankin@imperial.ac.uk*

## AA-CVD reactor for synthesis of photoelectrodes

Aerosol-assisted chemical vapour deposition (AA-CVD) synthesis was conducted in a purpose-build reactor (shown in **Figure S1**). The temperature of the reaction chamber was controlled by heating a graphitic carbon block (Olmec). Holes were drilled in the carbon for a WATLOW G10A32-L12 heating rod (750 W, Sensemaster) and two thermocouples (RS components). The desired temperature of the reaction was controlled by a temperature control unit (Eurotherm and Tempatron controller) communicating with the heating rod and thermocouples.

The precursor was injected into a two-necked round bottom flask and the aerosol was generated using an ultrasonic humidifier (2 MHz, Liquifog, Johnson Matthey).

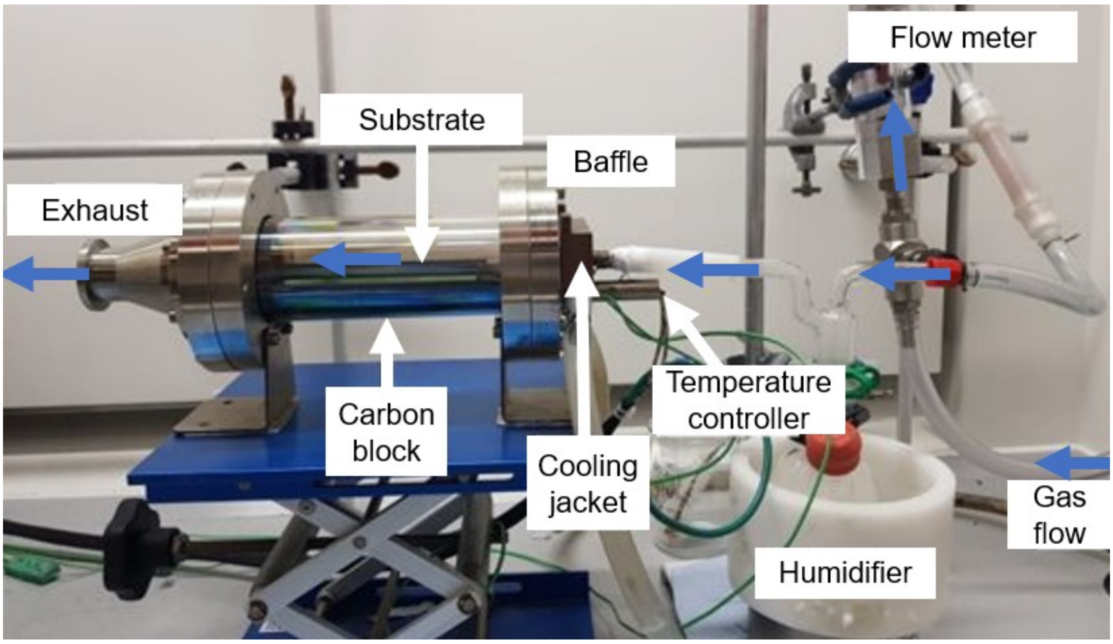

**Figure S1.** The purpose-built AA-CVD reactor used for the synthesis of photoelectrode materials.

## Light source characterisation

Light sources used for photoelectrochemical characterisation, measured using StellarNet Black Comet and Dwarf Star photospectrometers and compared to the NREL AM 1.5G reference spectrum [1].

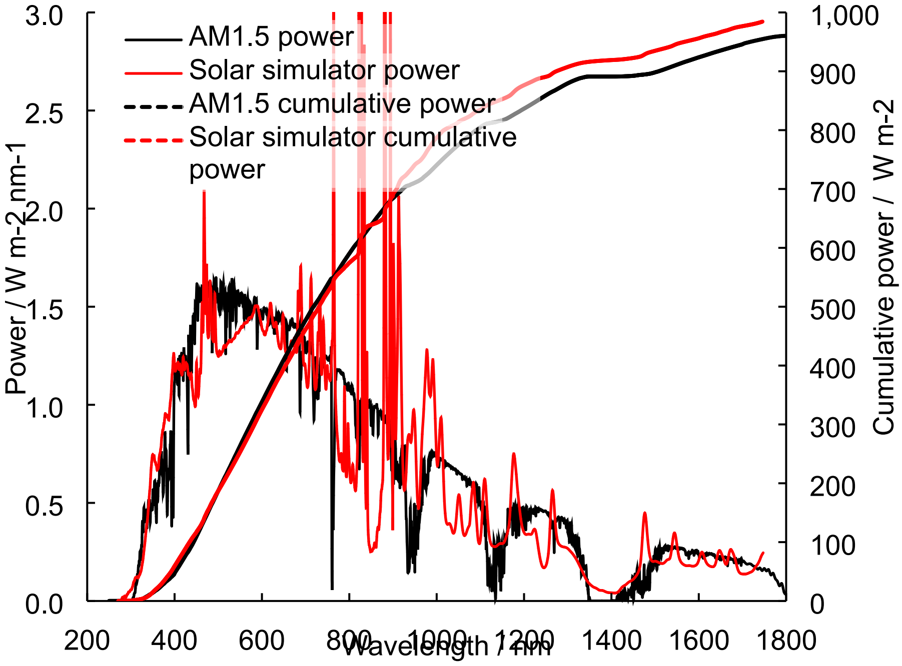

**Figure S2.** Spectrum of Sun2000 Solar Simulator measured by StellarNet Black Comet and Dwarf Star photospectrometers, compared to NREL AM 1.5G reference spectrum [1].

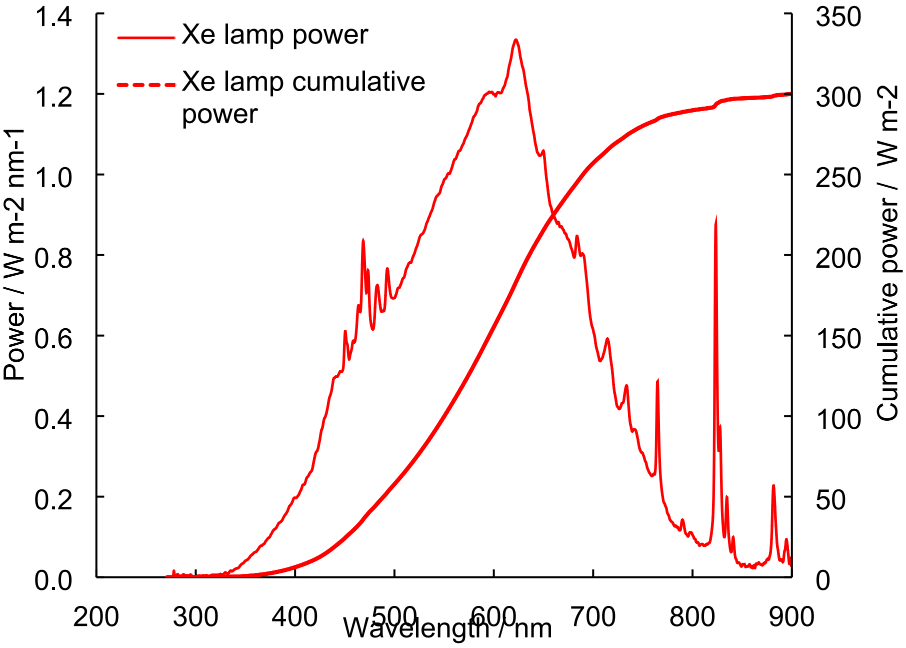

**Figure S3**. Spectrum of 75 W Xe lamp source measured by StellarNet Black Comet spectrophotometer.

**Table S1. Scheme of the tungsten trioxide ($WO_3$), bismuth vanadate ($BiVO_4$) and $WO_3$ | $BiVO_4$ heterojunction samples tested in this study.**

| | |
|---|---|
| | **$BiVO_4$ (synthesised at 400°C)**<br> |
| **$WO_3$ planar (synthesised at 325°C)**<br> | **$WO_3$ (planar) \| $BiVO_4$ heterojunction**<br>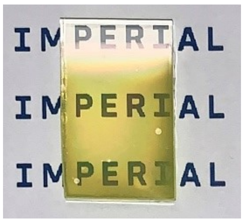 |
| **$WO_3$ hybrid (synthesised at 350°C)**<br> | **$WO_3$ (hybrid) \| $BiVO_4$ heterojunction**<br>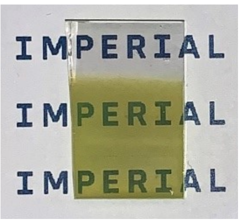 |
| **$WO_3$ nanoneedles (synthesised at 325°C)**<br> | **$WO_3$ (nanoneedles) \| $BiVO_4$ heterojunction**<br>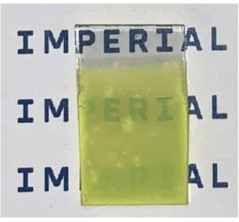 |

## Section 1: Preliminary PEC stability testing on planar $BiVO_4$ and nanoneedle $WO_3$ | $BiVO_4$ heterojunction photoanodes

Physical materials characterisation of $WO_3$, $BiVO_4$ and $WO_3$ | $BiVO_4$

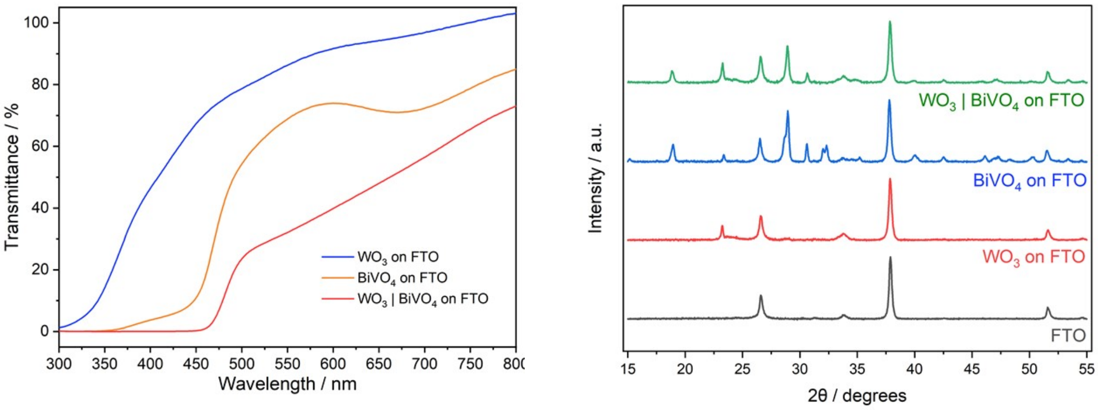

**Figure S4.** XRD pattern (left) and UV-Vis transmittance (right) of $WO_3$, $BiVO_4$ and $WO_3$ | $BiVO_4$ deposited on FTO.

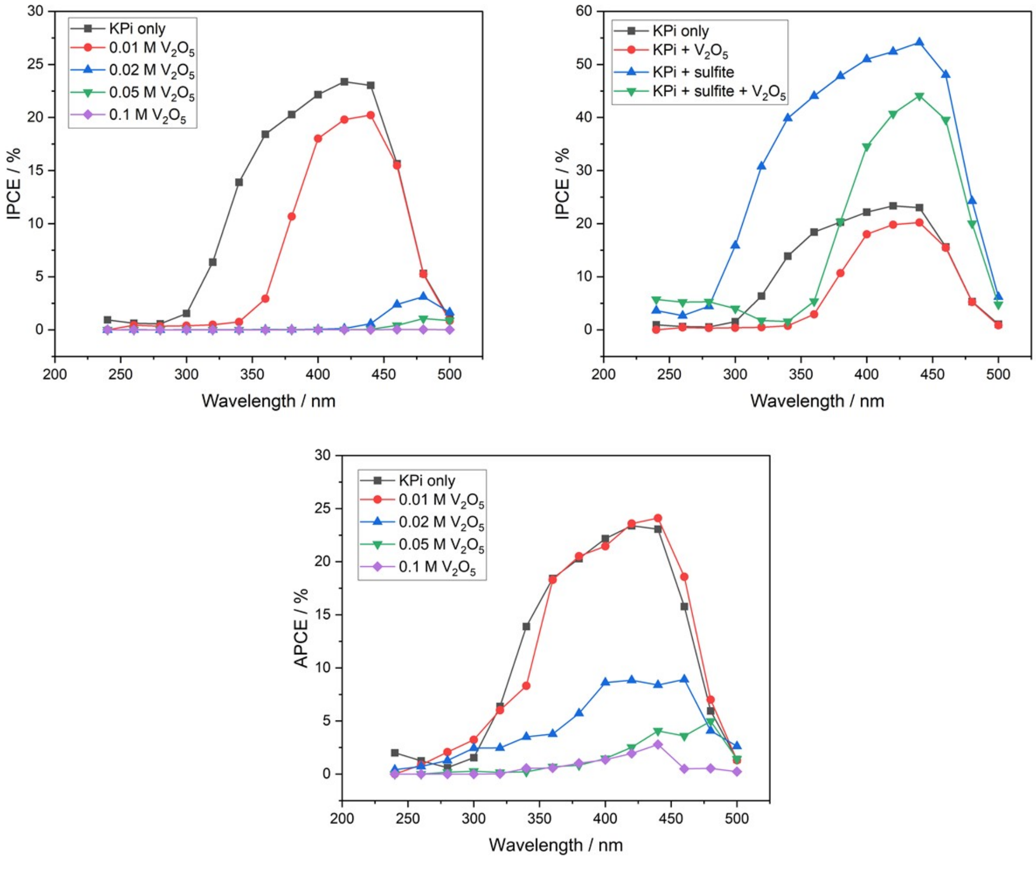

**Figure S5.** Incident photon to current efficiency for a $WO_3$ | $BiVO_4$ electrode in 0.1 M KPi (pH 7), electrolyte compared with the addition of various concentrations of $V_2O_5$ (top left) and with the addition of $V_2O_5$ and 0.5 M sodium sulfite hole scavenger (top right). Absorbed photon to current efficiency for a $WO_3$ | $BiVO_4$ electrode in various electrolytes (bottom).

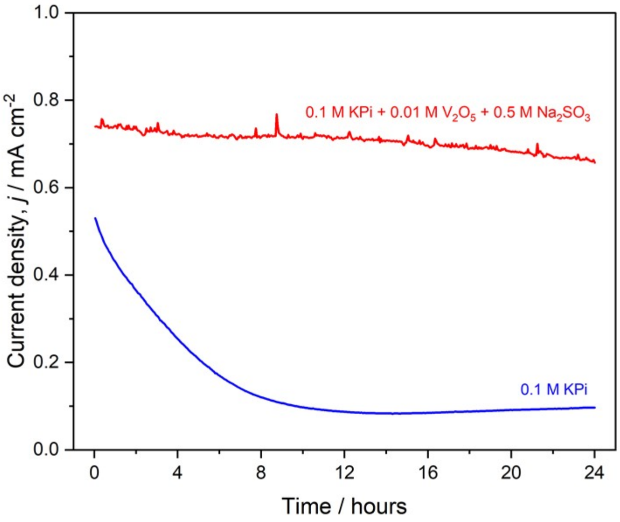

**Figure S6.** Chronoamperometry stability testing of $WO_3$ | $BiVO_4$ electrodes at 1.23 $V_{RHE}$ in 0.1 M KPi (pH 7) with 0.01 M $V_2O_5$ and 0.5 M $Na_2SO_3$ compared with 0.1 KPi only. PEC measurements were taken under simulated sunlight a 75 W Xe light source equipped with a KG3 filter with equivalent light intensity of 0.42 suns.

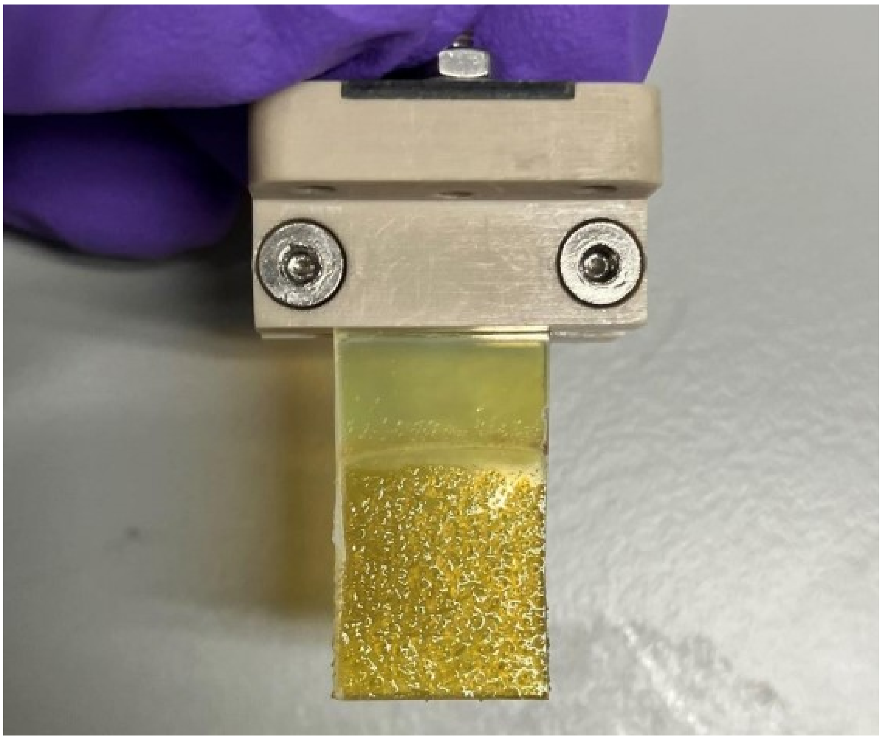

**Figure S7.** Precipitation of vanadium(V) salt on the immersed area of the $WO_3$ | $BiVO_4$ photoanode after 24 hours PEC stability testing at 1.23 $V_{RHE}$ in 0.1 M KPi + 0.1 M $V_2O_5$ electrolyte.

## Section 2: Optimisation of the $WO_3$ morphology for improved photoanode mechanical stability

### HR-TEM characterisation of $WO_3$

High resolution transmission electron microscopy (HR-TEM) analysis was carried out on a $WO_3$ nanoparticle from a $WO_3$ film prepared by AA-CVD at 350°C. This showed that the as-synthesised $WO_3$ is highly crystalline in nature with primary lattice spacing of 3.62 Å and 3.91 Å, which correspond to the (200) and (002) crystal planes, similarly to $WO_3$ nanoneedles synthesised at 325°C and 375°C [2–4].

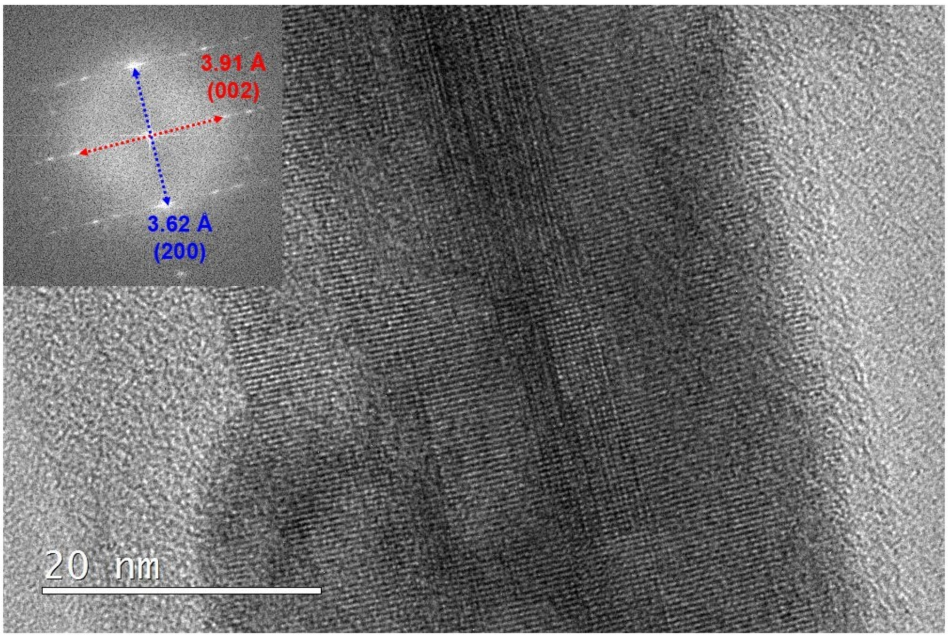

**Figure S8.** HR-TEM image (300 000 times magnification) of a $WO_3$ nanoparticle from a $WO_3$ film prepared by AA-CVD at 350°C, with accompanying diffraction pattern analysis.

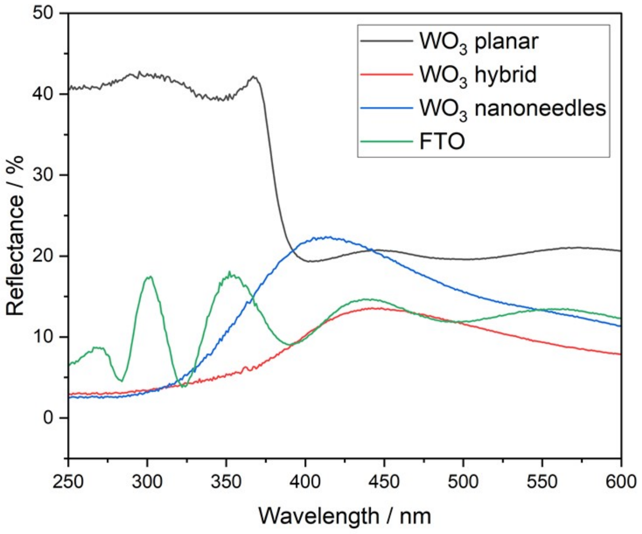

**Figure S9.** UV-Vis reflectance of $WO_3$ electrodes, compared with FTO.

## Section 3: Development of a NiFeOOH co-catalyst using a scalable CVD method

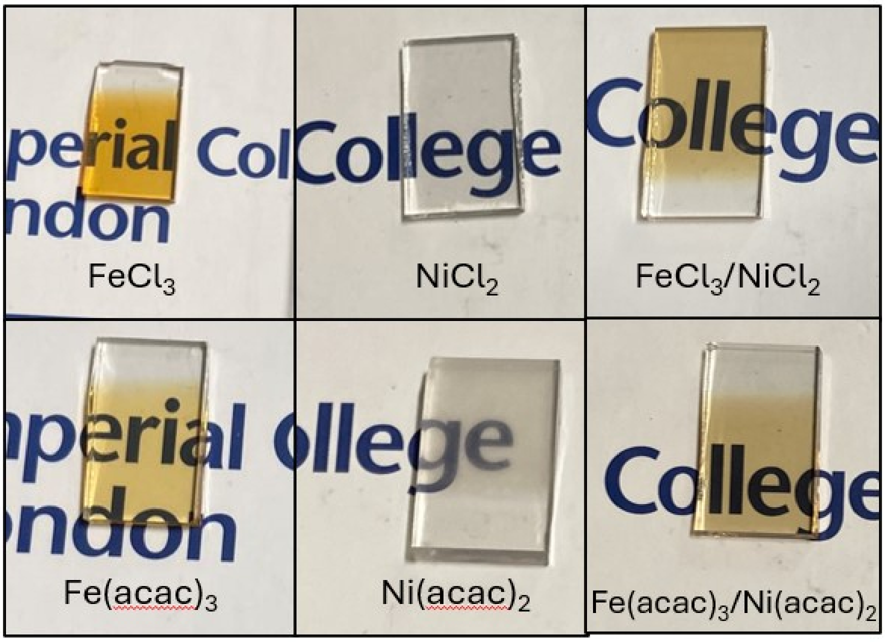

**Figure S10.** Nickel and iron based water oxidation surface co-catalysts, deposited on FTO for physical materials characterisation. A volume of 500 mL of each precursor was passed through the AA-CVD chamber. Iron precursors had a concentration of 1 mM and nickel precursors had a concentration of 4 mM. In the case of mixed precursors, the iron and nickel constituents had a concentration of 1 mM and 4 mM, respectively.

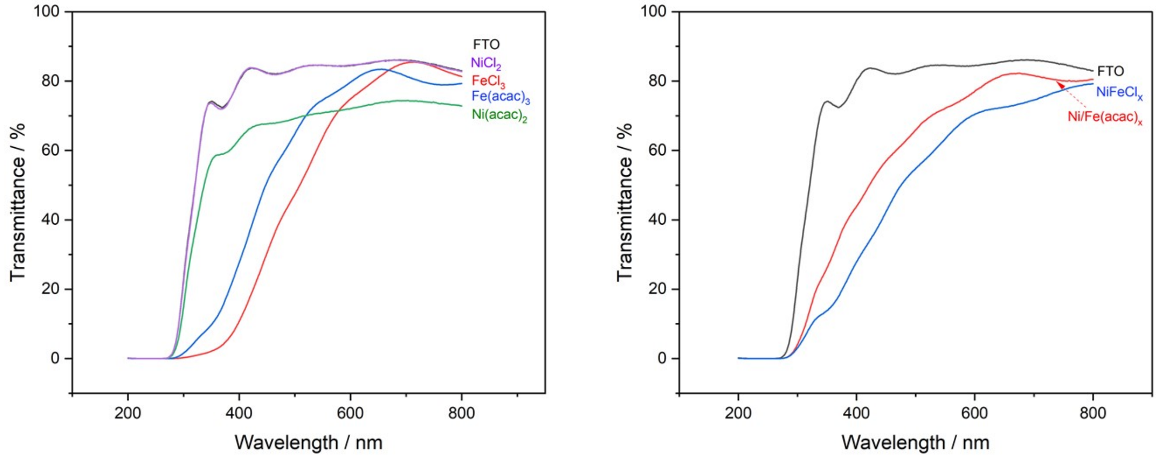

**Figure S11.** UV-vis transmittance of co-catalyst films deposited from $Ni(acac)_2$, $Fe(acac)_3$, $FeCl_3$ and $NiCl_2$ precursors (left) and mixed chloride and acetylacetonate precursors (right).

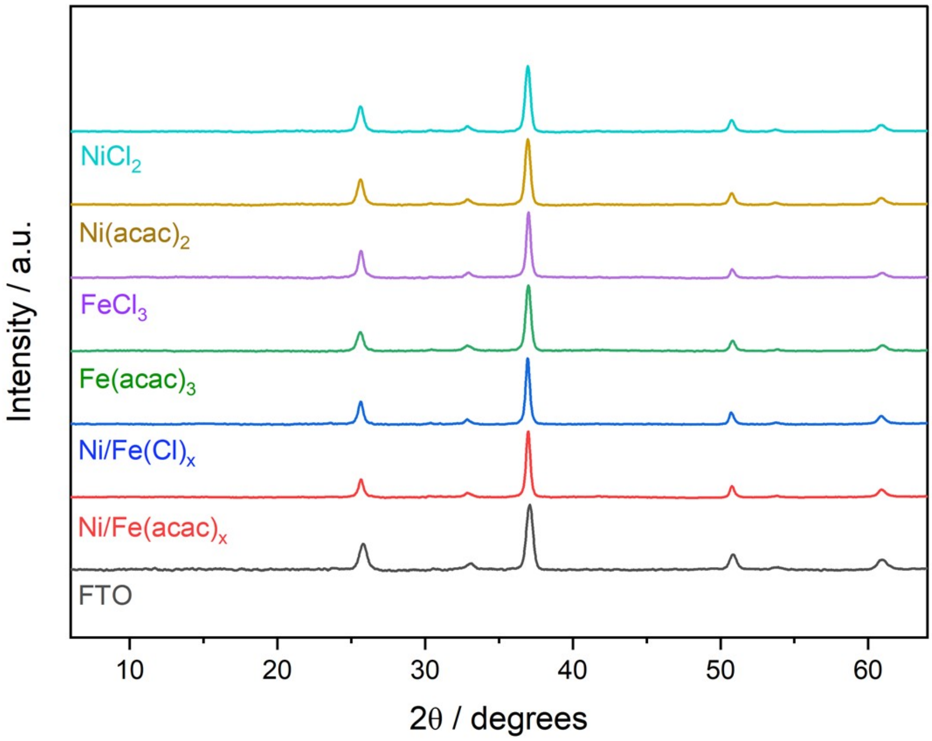

**Figure S12.** XRD analysis of co-catalyst films deposited on FTO from Ni(acac)$_2$, Fe(acac)$_3$ and FeCl$_3$ and NiCl$_2$ precursors showing no additional peaks compared to FTO, confirming their amorphous nature.

HR-TEM of the WO$_3$ | BiVO$_4$ | NiFeOOH material is shown in **Figure S13**. A significant proportion of the surface of the material appeared highly amorphous, as a result of NiFeOOH on the surface. However, HR-TEM showed that the as-synthesised monoclinic scheelite BiVO$_4$ was highly crystalline with primary lattice spacing of 3.01 Å, corresponding to the (121) crystal plane [5].

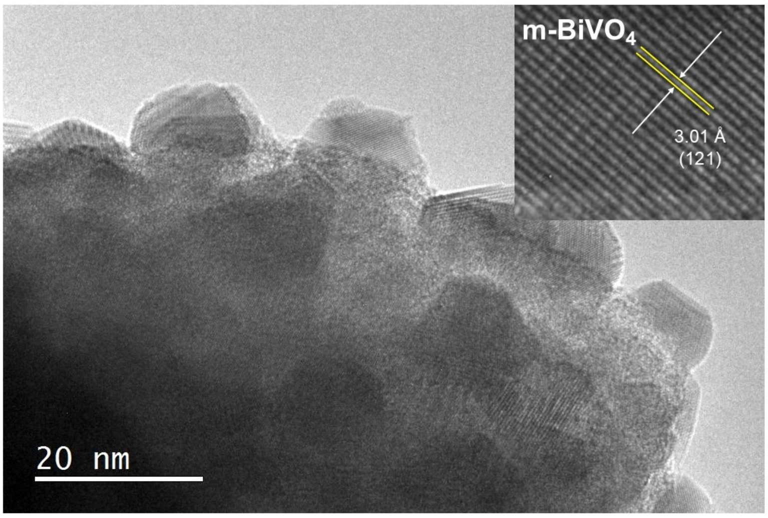

**Figure S13.** HR-TEM image (350 000 times magnification) of $WO_3$ | $BiVO_4$ | NiFeOOH and lattice spacing of a $BiVO_4$ nanoparticle (inset).

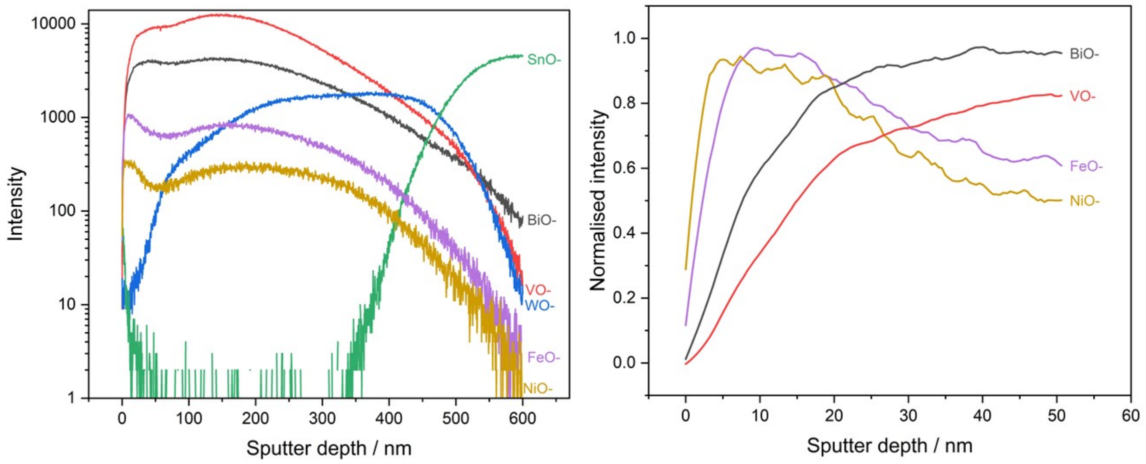

**Figure S14**. Time-of-flight secondary ion mass spectrometry (ToF-SIMS) of a $WO_3$ | $BiVO_4$ | NiFeOOH electrode. Full layer profile of the material, illustrated by representative signals (left) and NiFeOOH layer profile, illustrated by representative signals (right).

**Figure S15** (overleaf) shows XPS analysis of a representative $WO_3$ | $BiVO_4$ | NiFeOOH sample. Binding energies were referenced by the adventitious carbon (C-C) peak seen in the C 1s binding energy region (shown in **Figure S15a**). The C 1s environment gave rise to three peaks at 284.8 eV, 286.6 eV and 288.5 eV, corresponding to (C-C), (C-O) and (C=O) components and manifest because of adventitious carbon contamination [6]. The Bi 4f environment (shown in **Figure S15b**) gave rise to peaks at 159.4 eV and 164.7 eV, corresponding to the 7/2 and 5/2 peaks of $Bi^{3+}$ [7]. There were also peaks at 157.8 eV and 163.4 eV, which are the likely cause of preferential reduction of bismuth during the XPS experiment, from the $Bi^{3+}$ oxidation state to metallic $Bi^0$ and bismuth-based impurity compounds (e.g. $Bi_2S_3$) [8]. In the V 2p environment (shown in **Figure S15c**) there were two peaks at 517.0 eV and 524.5 eV, corresponding to the 3/2 and 1/2 peaks of $V^{5+}$ [9]. This provides verification that the bismuth and vanadium components are in the expected oxidation states for pure $BiVO_4$. Analysis of the O 1s environment (shown in **Figure S15d**) suggested the presence of several metal-oxygen (M-O) components, which resulted due to Bi, V, W, Ni and Fe oxides. This makes the deconvolution uncertain and therefore these components are represented by a single peak at 530.3 eV. A second peak at 532.0 eV represents the (C-O) component of adventitious carbon. In the W 4f environment (shown in **Figure S15e**), there were two peaks at 35.5 eV and 37.7 eV, which correspond to the 7/2 and 5/2 peaks of $W^{6+}$, providing evidence for the expected oxidation state of tungsten for $WO_3$ [10].

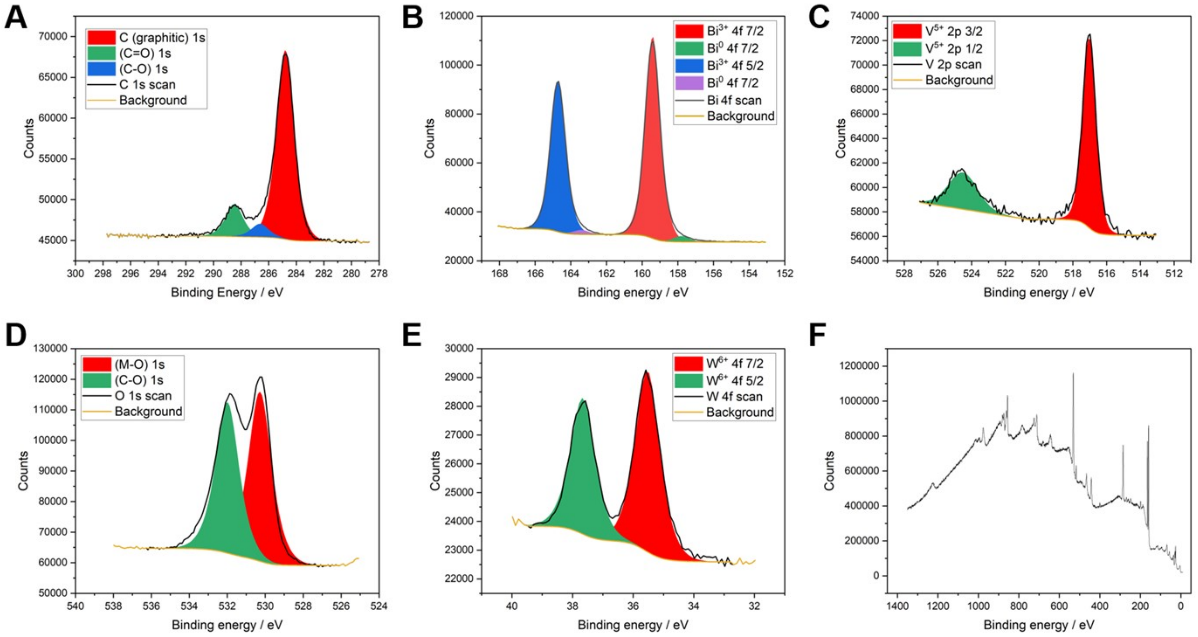

**Figure S15.** XPS analysis of the C 1s (A), Bi 4f (B), V 2p (C), O 1s (D), W 4f (E) environments and XPS survey (F) of a $WO_3$ | $BiVO_4$ | NiFeOOH sample deposited on FTO.

Due to the number of overlapping peaks in NiOOH and FeOOH XPS spectra, the -OOH components are typically characterised by comparing features that are typically present in other nickel/iron oxide and hydroxide XPS spectra. In the Ni 2p environment, the multiplet splitting and maximum peak position can be used to distinguish between possible nickel oxide or hydroxide components. As **Figure S16a** shows, the characteristic NiO peak at 854.5 eV is absent, showing that this component is not present in the material [11]. The shape of the curve is also analogous with previously reported Ni 2p spectra of β- and γ-NiOOH [12,13]. The maximum peak at 856.0 eV is indicative of a NiOOH and $Ni(OH)_2$ mixture in line with previous literature, which has shown that the exact composition of the mixture can be tuned, if desired, through electrochemical conditioning [11,13]. The Fe 2p environment (shown in **Figure S16b**) provides evidence of the successful loading of Fe, with the shape and major peaks at 724.6 eV and 711.3 eV in line with previous reports for β-FeOOH [14–16]. The presence of the characteristic Fe 2p 3/2 satellite peak at 720.0 eV suggests that the primary component in the Fe 2p region is $Fe^{3+}$ [14,15]. This, along with evidence provided earlier from UV-Vis analysis, confirms the successful loading of NiFeOOH.

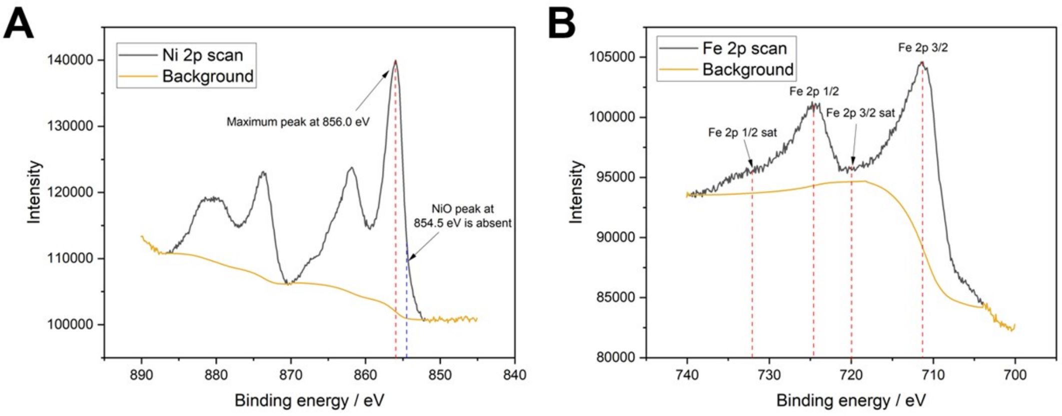

**Figure S16.** XPS analysis of the Ni 2p (A) and Fe 2p (C) environments of a $WO_3$ | $BiVO_4$ | NiFeOOH sample deposited on FTO.

**Photoelectrochemical characterisation of the optimised photoanode system**

**Figure S17** shows the photocurrent density of $WO_3$ | $BiVO_4$ electrodes during chopped chronoamperometry measurements at 1.23 $V_{RHE}$.

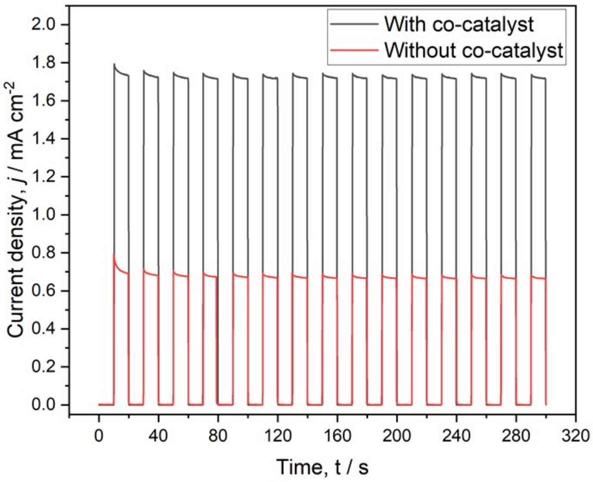

**Figure S17.** Chronoamperometry measurements at 1.23 $V_{RHE}$ in 1 M borate buffer (pH 9) for two $WO_3$ | $BiVO_4$ electrodes with and without NiFeOOH surface co-catalyst. AM 1.5 G light (1000 W $m^{-2}$) was mechanically chopped at 10 second intervals.

Calculating the estimated interfacial charge transfer efficiency (charge injection efficiency) using the relation between the initial and stable photocurrent densities (eqn. 7) resulted in values of 95.5% and 98.4% for the samples with and without NiFeOOH co-catalyst. These efficiencies were obtained by taking the average over all 15 transients, with the efficiency calculated from each transient presented in **Table S2**. These were considerably higher than the values calculated using the sacrificial electrolyte method previously.

We believe that the large discrepancy between the interfacial charge transfer efficiency between the chopped chronoamperometry method and the sacrificial electrolyte method is due to the use of a Xe arc lamp with mechanically chopped light. Unfortunately, these light sources are unsuitable for transient photocurrent measurements in the order of milliseconds, as this requires almost instantaneous switching from light and dark to obtain reliable and reproducible results [17]. The dynamics of the photocurrent are faster than the mechanics of the light simulator. Xe arc lamps cannot be powered up on down in the order of milliseconds, requiring the use of a mechanical chopper to switch between light and dark. The use of a mechanical chopper results in the very brief (millisecond scale) partial illumination of the sample, which reduces spikes in photocurrent that result from the competition between recombination and interfacial charge transfer processes [18,19]. The discrepancy herein highlights the importance of validating data with multiple experimental methods where possible, and having an understanding of the equipment limitations, since in this instance, the charge transfer efficiency calculated using the transient photocurrent method was significantly overestimated.

**Table S2.** Calculated interfacial charge transfer efficiency of $WO_3$ | $BiVO_4$ with and without co-catalyst, based on transient chronoamperometry measurements.

| | $\phi_{inj} = {J_{ph,t\rightarrow\infty}}/{J_{ph,t=0}}$ | |
|---|---|---|
| **Repeat (n)** | **No co-catalyst** | **With co-catalyst** |
| 1 | 0.815 | 0.965 |
| 2 | 0.953 | 0.980 |
| 3 | 0.956 | 0.982 |
| 4 | 0.965 | 0.983 |
| 5 | 0.966 | 0.984 |
| 6 | 0.966 | 0.988 |
| 7 | 0.945 | 0.984 |
| 8 | 0.969 | 0.985 |
| 9 | 0.964 | 0.990 |
| 10 | 0.969 | 0.989 |
| 11 | 0.969 | 0.986 |
| 12 | 0.973 | 0.985 |
| 13 | 0.968 | 0.985 |
| 14 | 0.971 | 0.990 |
| 15 | 0.973 | 0.988 |
| **Average, n = 15** | **0.955 ± 0.038** | **0.984 ± 0.005** |
| **Average, n = 14 (excluding first)** | **0.965 ± 0.007** | **0.986 ± 0.002** |

**Table S3.** Resistance and capacitance values of $WO_3$ | $BiVO_4$ with and without NiFeOOH, obtained by PEIS modelling at 0.8 $V_{RHE}$.

| **Electrode** | **$R_{\text{Faradaic}}$ / Ω** | **$R_{\text{HF}}$ / Ω** | **$C_{\text{HF}}$ / µF** | **$R_{\text{LF}}$ / Ω** | **$C_{\text{LF}}$ / mF** |
|---|---|---|---|---|---|
| *$WO_3$ \| $BiVO_4$* | 108 | 124 | 211 | 137 | 7.33 |
| *$WO_3$ \| $BiVO_4$ \| NiFeOOH* | 108 | 181 | 119 | 4340 | 2.12 |

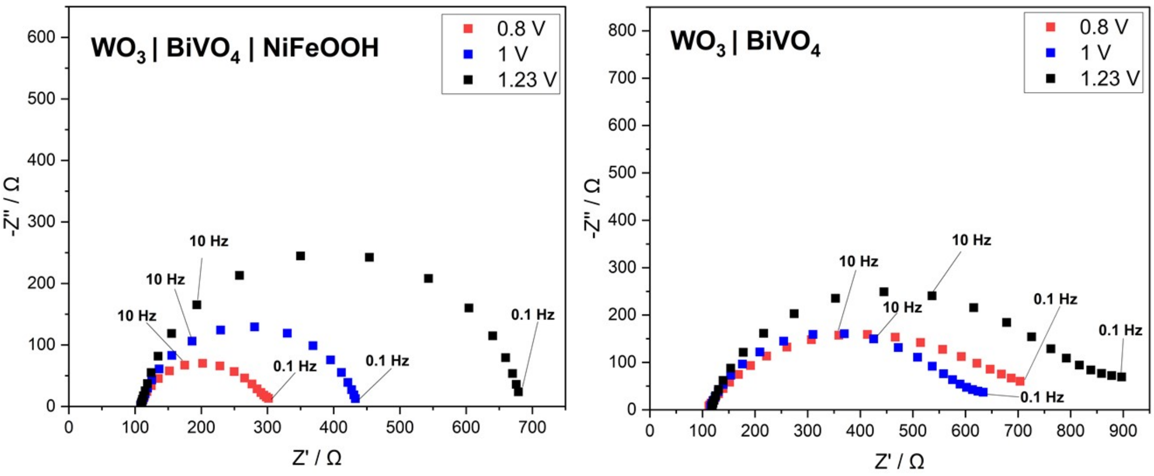

**Figure S18.** Nyquist plots of WO$_3$ | BiVO$_4$ (left) and WO$_3$ | BiVO$_4$ | NiFeOOH (right) electrodes from PEIS measurements at various potentials and frequencies.

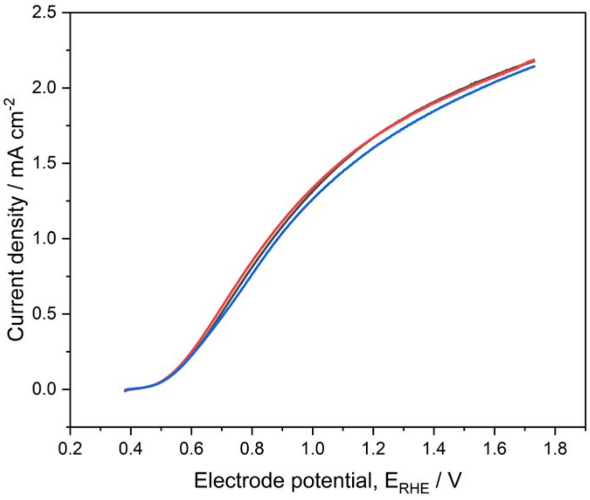

**Figure S19.** Linear sweep voltammograms of three WO$_3$ | BiVO$_4$ | NiFeOOH electrodes, synthesised using the same AA-CVD method under continuous illumination.

## Section 4: Evaluating the mechanical and photoelectrochemical stability of the fully optimised WO$_3$ | BiVO$_4$ | NiFeOOH photoanode system

### SEM images from WO$_3$|BiVO$_4$|NiFeOOH stability testing:

SEM images (shown in **Figure S19**) of as synthesised WO$_3$|BiVO$_4$|NiFeOOH electrodes and WO$_3$|BiVO$_4$|NiFeOOH electrodes after a 24 hour stability test showed that the experiment resulted in no visible morphological changes.

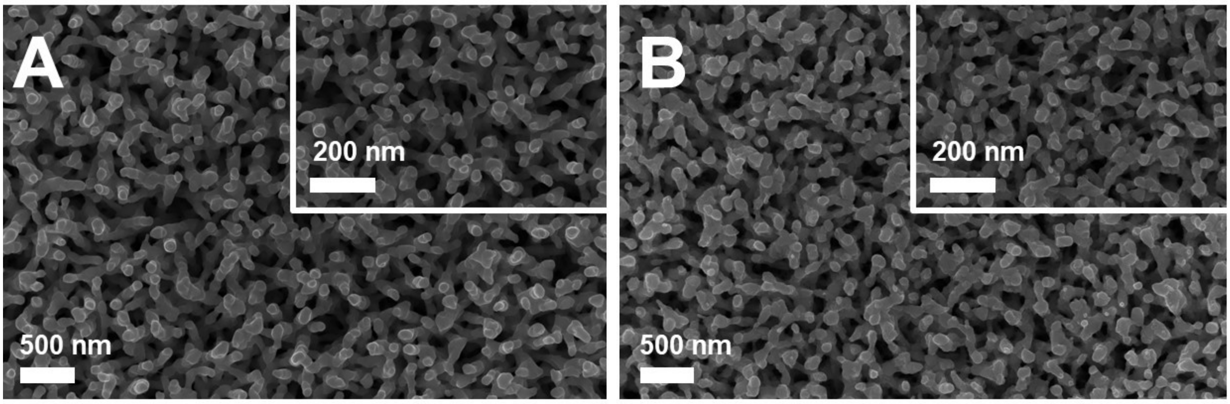

**Figure S20.** SEM images of an as-synthesised $WO_3|BiVO_4|$NiFeOOH photoanode, captured before (A) and after (B) 24 hour chronoamperometry testing at 1.23 $V_{RHE}$ in 1 M borate buffer with an electrolyte flowrate of 40 mL min$^{-1}$. Main image magnification: 50 kX. Inset image magnification: 100 kX.

## References

1 NREL, Resource Spectra AM 1.5, https://www.nrel.gov/grid/solar-resource/spectra-am1.5.html, (accessed 20 December 2024).

2 B. Gerand, G. Nowogrocki, J. Guenot and M. Figlarz, *J Solid State Chem*, 1979, 29, 429–434.

3 C. Reddick, C. Sotelo-Vazquez, B. Tam, A. Kafizas, K. Reynolds, S. Stanley, G. Creasey, A. Hankin, C. Pablos and J. Marugán, *Catal Today*, 2024, 437, 114783.

4 A. Kafizas, L. Francàs, C. Sotelo-Vazquez, M. Ling, Y. Li, E. Glover, L. McCafferty, C. Blackman, J. Darr and I. Parkin, *J Phys Chem C*, 2017, 121, 5983–5993.

5 G. S. Kamble and Y.-C. Ling, *Sci Rep*, 2020, 10, 12993.

6 A. Shchukarev and D. Korolkov, *Open Chem*, 2004, 2, 347–362.

7 W. E. Morgan, W. J. Stec and J. R. Van Wazer, *Inorg Chem*, 1973, 12, 953–955.

8 T. P. Debies and J. W. Rabalais, *Chem Phys*, 1977, 20, 277–283.

9 B. Barbaray, J. P. Contour and G. Mouvier, *Environ Sci Technol*, 1978, 12, 1294–1297.

10 S. F. Ho, S. Contarini and J. W. Rabalais, *J Phys Chem*, 1987, 91, 4779–4788.

11 N. Weidler, J. Schuch, F. Knaus, P. Stenner, S. Hoch, A. Maljusch, R. Schäfer, B. Kaiser and W. Jaegermann, *J Phys Chem C*, 2017, 121, 6455–6463.

12 A. P. Grosvenor, M. C. Biesinger, R. St. C. Smart and N. S. McIntyre, *Surf Sci*, 2006, 600, 1771–1779.

13 J. Gallenberger, H. Moreno Fernández, A. Alkemper, M. Li, C. Tian, B. Kaiser and J. P. Hofmann, *Catal Sci Technol*, 2023, 13, 4693–4700.

14 J. Cui, M. Daboczi, M. Regue, Y. Chin, K. Pagano, J. Zhang, M. A. Isaacs, G. Kerherve, A. Mornto, J. West, S. Gimenez, J. Kim and S. Eslava, *Adv Funct Mater*, 2022, 32, 2207136.

15 W. Zhang, J. Ma, L. Xiong, H.-Y. Jiang and J. Tang, *ACS Appl Energy Mater*, 2020, 3, 5927–5936.

16 T. Zhou, S. Chen, J. Wang, Y. Zhang, J. Li, J. Bai and B. Zhou, *Chem Eng J*, 2021, 403, 126350.

17 L. M. Peter, *J Solid State Electrochem*, 2013, 17, 315–326.

18 F. E. Bedoya-Lora, M. E. Valencia-García, A. Hankin, D. Klotz and J. A. Calderón, *Electrochim Acta*, 2022, 402, 139559.

19 F. E. Bedoya-Lora, I. Holmes-Gentle and A. Hankin, *Curr Opin Green Sustain Chem*, 2021, 29, 100463.